

Article

Building Low-Cost, High-Performance Flexible Photodetector Based on Tetragonal Phase VO₂ (A) Nanorod Networks

Wenhui Lin ¹, Chaoyang Tang ¹, Feiyu Wang ¹, Yiyu Zhu ¹, Zhen Wang ¹, Yifan Li ¹, Qiuqi Wu ¹, Shuguo Lei ¹, Yi Zhang ^{2,*}  and Jiwei Hou ^{1,*} 

¹ Department of Physics, School of Physical and Mathematical Science, Nanjing Tech University, Nanjing 211816, China; 13588028173@163.com (W.L.); tcyofficial@njtech.edu.cn (C.T.); fywang0907@163.com (F.W.); yiyuzhu@njtech.edu.cn (Y.Z.); zhenwang@njtech.edu.cn (Z.W.); 202161121005@njtech.edu.cn (Y.L.); 202021154023@njtech.edu.cn (Q.W.); sglei@njtech.edu.cn (S.L.)
² School of Energy Science and Engineering, Nanjing Tech University, Nanjing 211816, China
* Correspondence: zhangyi@njtech.edu.cn (Y.Z.); jwhou@njtech.edu.cn (J.H.)

Abstract: We present a straightforward and cost-effective method for the fabrication of flexible photodetectors, utilizing tetragonal phase VO₂ (A) nanorod (NR) networks. The devices exhibit exceptional photosensitivity, reproducibility, and stability in ambient conditions. With a 2.0 V bias voltage, the device demonstrates a photocurrent switching gain of 1982% and 282% under irradiation with light at wavelengths of 532 nm and 980 nm, respectively. The devices show a fast photoelectric response with rise times of 1.8 s and 1.9 s and decay times of 1.2 s and 1.7 s for light at wavelengths of 532 nm and 980 nm, respectively. In addition, the device demonstrates exceptional flexibility across large-angle bending and maintains excellent mechanical stability, even after undergoing numerous extreme bending cycles. We discuss the electron transport process within the nanorod networks, and propose a mechanism for the modulation of the barrier height induced by light. These characteristics reveal that the fabricated devices hold the potential to serve as a high-performance flexible photodetector.

Keywords: tetragonal phase VO₂ (A); low-cost; high-sensitivity photoresponse; flexible photodetector



Citation: Lin, W.; Tang, C.; Wang, F.; Zhu, Y.; Wang, Z.; Li, Y.; Wu, Q.; Lei, S.; Zhang, Y.; Hou, J. Building Low-Cost, High-Performance Flexible Photodetector Based on Tetragonal Phase VO₂ (A) Nanorod Networks. *Materials* **2023**, *16*, 6688. <https://doi.org/10.3390/ma16206688>

Academic Editor: Giuseppe Mele

Received: 24 August 2023

Revised: 30 September 2023

Accepted: 10 October 2023

Published: 14 October 2023



Copyright: © 2023 by the authors. Licensee MDPI, Basel, Switzerland. This article is an open access article distributed under the terms and conditions of the Creative Commons Attribution (CC BY) license (<https://creativecommons.org/licenses/by/4.0/>).

1. Introduction

One-dimensional semiconducting nanostructures, such as nanowires, nanotubes, nanobelts, and nanoribbons, have captured considerable attention owing to their novel physical and chemical properties and potential applications in nanoscale electronics and optoelectronics [1–3]. They are characterized by a significant surface-to-volume ratio, a high aspect ratio, easy surface functionalization, and a unique electron-limited domain effect, which can extend the lifetime of photogenerated carriers [4]. Additionally, their linear geometrical structure provides them with good elasticity against external stresses, and they are less prone to cracking after deformation. These features make one-dimensional semiconductor nanowires ideal for designing and preparing high-performance photodetector devices. Many high-performance photodetectors utilizing one-dimensional semiconductor nanostructures, such as ZnO, Zn₂GeO₄, SnO₂, and V₂O₅ have been prepared [5–7]. Among the variety of 1D semiconductor nanostructures, Vanadium dioxide (VO₂) exhibits a reversible metal-insulator transition at 68 °C, where its crystal structure changes from a monoclinic phase at low temperatures to a rutile-type tetragonal phase at high temperatures, accompanied by significant changes in its electrical, magnetic, and optical properties. These novel properties enable a broad array of applications for VO₂, including photodetectors, actuators, gas sensors, Mott-effect transistors and smart windows [8–10].

VO₂ serves as a typical binary compound with multiple polymorphisms, such as VO₂ (B), VO₂ (A), VO₂ (M1), and VO₂ (R) [11,12]. These distinct polycrystalline structures

have different properties and many different applications. For instance, due to its layered crystal structure, VO₂ (B) is often used as a potential high-performance lithium battery electrode material in energy storage applications. Due to the robustness and durability of the structure and the unique open channels for Li-ion conduction, epitaxially grown VO₂ (B) films can reach the theoretical limit of capacity through its sustained charge/discharge cycling capability [13]. VO₂ (M1) and VO₂ (R) have reversible metal-insulator phase transition properties and high temperature resistance coefficients, making them suitable for infrared photodetectors, optical switches, and smart windows [14,15]. Over the past few decades, substantial research efforts have been directed towards the comprehensive investigation of the syntheses, features, and potential applications of VO₂ (B) and VO₂ (M1), VO₂ (R). However, there have been fewer studies of other polymorphs in the VO₂ system that may also include unique physical and chemical characteristics as well as potential applications. Tetragonal phase vanadium dioxide, known as VO₂ (A), exhibits a comparable reversible phase transition around 162 °C; however, its electrical and optical properties have been sparsely reported due to insufficient attention [16]. The crystal structure of VO₂ (A) is constructed from interconnected three-dimensional arrays of VO₆ octahedra. It is noteworthy that the V-O spacing in the [110] orientation is smaller compared to the other directions, which favors its preferential growth along the one-dimensional direction. Several studies have recently been carried out on the physical properties and structure of tetragonal phase VO₂ (A). Belt-shaped VO₂ (A) with a rectangular profile was produced and exhibited good thermal stability in air [17]. Both theory and experiments have revealed that VO₂ (A) nanowires can be employed as H₂S gas sensors, showcasing exceptional selectivity and reproducibility [18]. The structural evolution of VO₂ (A) NRs under pressure reveals information about the VO₂ (A) phase transition [19]. Through an analysis of the electrical properties of VO₂ (A), its distinctive field emission characteristics have been elucidated [20]. VO₂ (A) serves as a semiconductor material with a suitable optical band gap. However, a comprehensive study of the complex optical and electrical properties of nanostructured VO₂ (A) remains a task to be undertaken. Consequently, the advancement of optoelectronic devices based on these materials requires an improved understanding of their photoresponse properties, and we herein investigate the optoelectronic characteristics of VO₂ (A) NR networks utilized in a photodetector.

The performance of a photodetector depends on the properties of its active material, including factors such as the absorption coefficient, bandgap width and morphology. Typically, multifunctional device fabrication involving nanostructures requires specialized substrate growth, which often requires a complex design process [21]. In this study, we demonstrate a low-cost flexible photodetector constructed with tetragonal phase VO₂ (A) NR networks, which exhibits highly sensitive photoresponse properties (rise and decay times of 1.8 and 1.2 s, respectively). The device can be repeatedly bent at large angles without experiencing a significant loss of photoresponse properties. We have explored the electron transfer process in NR networks, revealing the mechanism of photocurrent generation and the factors affecting the performance. These features indicate that the fabricated flexible devices have the potential to be used as high-performance photodetectors.

2. Experimental

2.1. Synthesis of Tetragonal Phase VO₂ (A) Nanorods

Tetragonal phase VO₂ (A) NRs were prepared through a hydrothermal method utilizing VOSO₄ as the precursor material, and the synthesis method was based on our previous report [11]. VOSO₄ was analytically pure and purchased from Shanghai Aladdin Biochemical Technology Co., Shanghai, China. Normally, VOSO₄ powder (0.08 g) was dispersed in 40 mL of deionized water (deionized water with a resistivity of 18.2 MΩ · cm was prepared in the laboratory), forming a clear blue solution after vigorous stirring. Subsequently, the blue solution was transferred into a 50 mL Teflon-lined autoclave housed within a stainless-steel shell and maintained at 220 °C for 24 h. After cooling the solution to ambient temperature, a brown slurry precipitate formed. After centrifugation, the

resulting precipitate was washed repeatedly with deionized water and ethanol. Ethanol was analytically pure and purchased from Shanghai Aladdin Biochemical Technology Co. This resulting precipitate underwent an overnight vacuum drying process at 60 °C for 8 h. Stable tetragonal phase VO₂ (A) NRs were obtained in the final experiment. No organic surfactants were introduced during the whole experiment.

2.2. Materials Characterization

The crystal structures of the acquired samples were analyzed through X-Ray diffraction (XRD) analyses conducted using a Smart-Lab diffractometer (Rigaku, Akishima, Japan) with a Cu-K α radiation source. The microstructures of samples were examined using a field emission scanning electron microscope (SEM, Hitachi S-4800, Tokyo, Japan). Transmission electron microscopy (TEM) images, including high-resolution TEM (HRTEM) images and selected area electron diffraction (SAED) patterns, were obtained for the samples using a TEM system (JEOL-2010, Akishima, Japan) operated at an acceleration voltage of 200 kV. Absorbance spectrum was obtained using a UV-VIS-NIR spectrophotometer (Shimadzu, UV-3700, Tokyo, Japan).

2.3. Fabrication of Tetragonal Phase VO₂ (A) Nanorod Networks Photodetector

During device fabrication, conventional UV lithography was used, followed by the deposition of gold electrodes (60 nm thick) on a polyethylene terephthalate (PET) substrate. Finally, the lift-off method was utilized to define the contact electrodes. The distance between the two gold electrodes measured approximately 15 μ m, and each gold electrode had a length of about 2 cm. Tetragonal phase VO₂ (A) NRs were suspended in deionized water using the ultrasonication process. The usual concentration maintained for this suspension was 0.2 mg/mL. The above solution was carefully deposited onto the pre-cleaned electrodes and allowed to air dry at ambient temperature. The device has been formed by a single-crystal VO₂ (A) NR networks. The electrical characteristics of the devices were carefully characterized under ambient conditions using a two-probe structure. To assure the precision and reliability of the measurements, a Keithley 4200 (Tektronix, Beaverton, OR, USA) semiconductor analyzer was used.

3. Results and Discussion

The scanning electron microscopy (SEM) analysis was conducted with a Hitachi S-4800 instrument to explore the morphology and microstructure of VO₂ (A) NRs. A typical scanning electron microscope image of tetragonal phase VO₂ (A) NRs is shown in Figure 1a, exhibiting lengths ranging in several tens of micrometers and widths of approximately 200 nm. The inset in Figure 1a is an SEM image at high magnification, providing a clearer view of the microstructure of the sample. The tetragonal phase VO₂ (A) exhibits a distinct rod-like morphology. High-resolution transmission electron microscopy (HRTEM) imaging, utilizing a JEOL-2010 instrument, confirms the single-crystalline quality of the NRs, as shown in Figure 1b. Different lattice fringes can be observed, with spacing between the neighboring fringes measuring 0.6 nm and 0.19 nm, effectively matching the spacing between the (110) and (004) lattice planes. This result is consistent with previous reports in the literature [22]. The inset of Figure 1b demonstrates a selected area electron diffraction (SAED) pattern characterized by a clear diffraction dot matrix structure, further confirming that the tetragonal phase VO₂ (A) NR is a single-crystal structure. Figure 1c shows the schematic diagram of the experimental configuration for performing the photoresponse measurements.

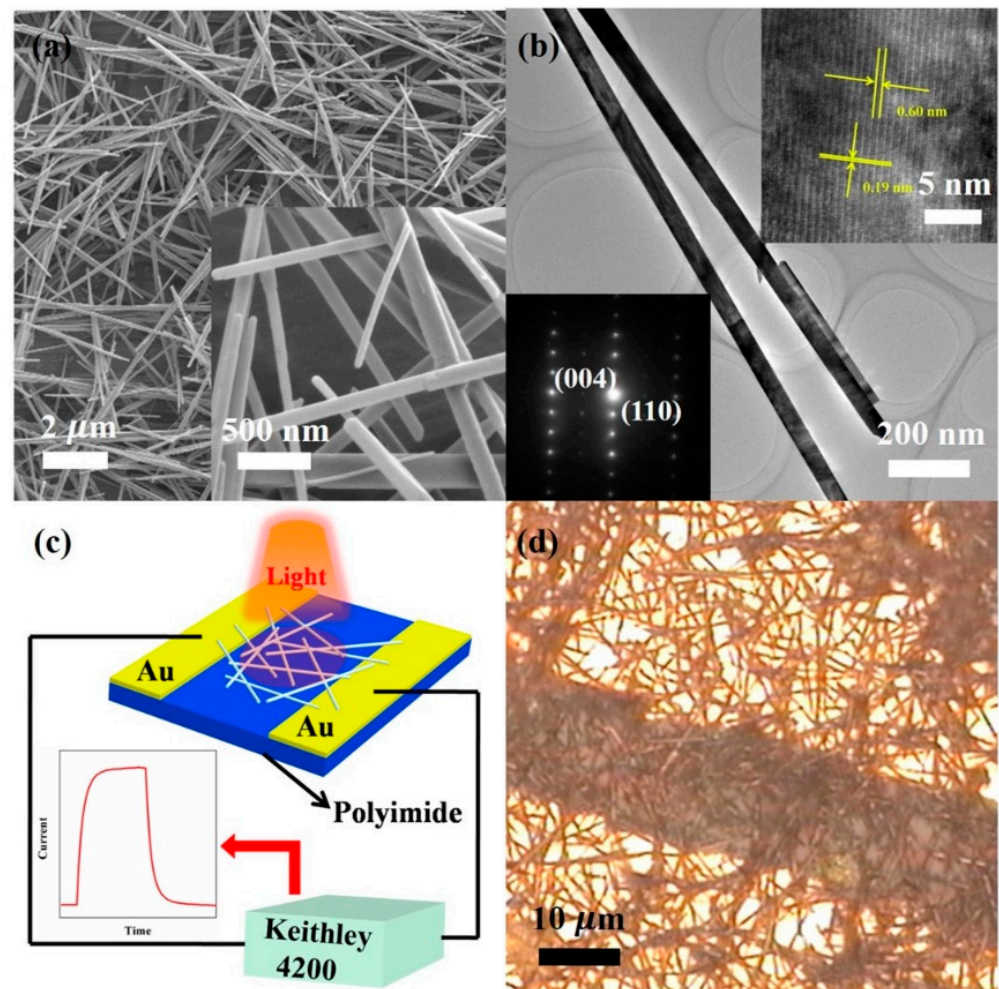


Figure 1. (a) Typical field-emission SEM (inset: high resolution SEM image, scale bar: 500 nm) image of tetragonal phase VO₂ (A) nanorods, scale bar: 2 μm. (b) TEM image of tetragonal phase VO₂ (A) nanorods (inset: the associated HRTEM image and SAED pattern, scale bar: 5 nm), scale bar: 200 nm. (c) Schematic diagram of the tetragonal phase VO₂ (A) nanorod network flexible photodetector. (d) Typical optical image of tetragonal phase VO₂ (A) nanorods.

VO₂ (A) NRs were dispersed on the PET substrate and formed a network structure connecting two gold electrodes. The dark currents and photocurrents resulting from vertically incident illumination were measured using a two-probe technique. The construction of our devices presents the advantages of simplicity, high performance, and cost-effectiveness in contrast to expensive and complex electron beam lithography. Figure 1d shows a photograph of a typical device, which consists of a dispersed VO₂ (A) NR network and two gold electrodes. The VO₂ (A) NRs are uniformly distributed in the gap between the gold electrodes, which have a width of 15 μm and a length of 2 cm, respectively.

The optical absorption spectrum of the tetragonal phase VO₂ (A) NR was recorded at room temperature utilizing a spectrophotometer (Shimadzu UV-3700). The UV-Vis-NIR absorption spectrum of the tetragonal phase VO₂ (A) NR is shown in Figure 2a. The optical absorption spectrum of the tetragonal phase VO₂ (A) NR shows a distinct absorption peak at 2.3 eV (538 nm). The current–voltage (I–V) characteristic curve is obtained by applying a bias voltage from −4.0 V to 4.0 V, as shown in Figure 2b. The photocurrent measurements were performed under laser irradiation at wavelengths of 532 nm and 980 nm, with laser power densities of 85 and 120 mW/cm², respectively. The photocurrent increased significantly under light, especially at high voltage bias. The I–V curves of the devices showed linear behavior both in the absence and presence of

light, indicating that the contact between the tetragonal phase VO₂ (A) NR and the gold electrode exhibits ohmic characteristics [23]. This indicates effective connectivity between the gold electrodes and the VO₂ (A) NR networks, with the junction resistance being comparatively smaller than the total device resistance. The dynamic photocurrent of the device under the irradiation of modulated visible and infrared light (532 nm and 980 nm) is shown in Figure 2c, where the modulation frequency of visible and infrared light is 10 seconds on and off. Under irradiation of visible and infrared optical power densities of 85 and 120 mW/cm², respectively, and a bias voltage of 2.0 V, the photodetector exhibited characteristic switching effects.

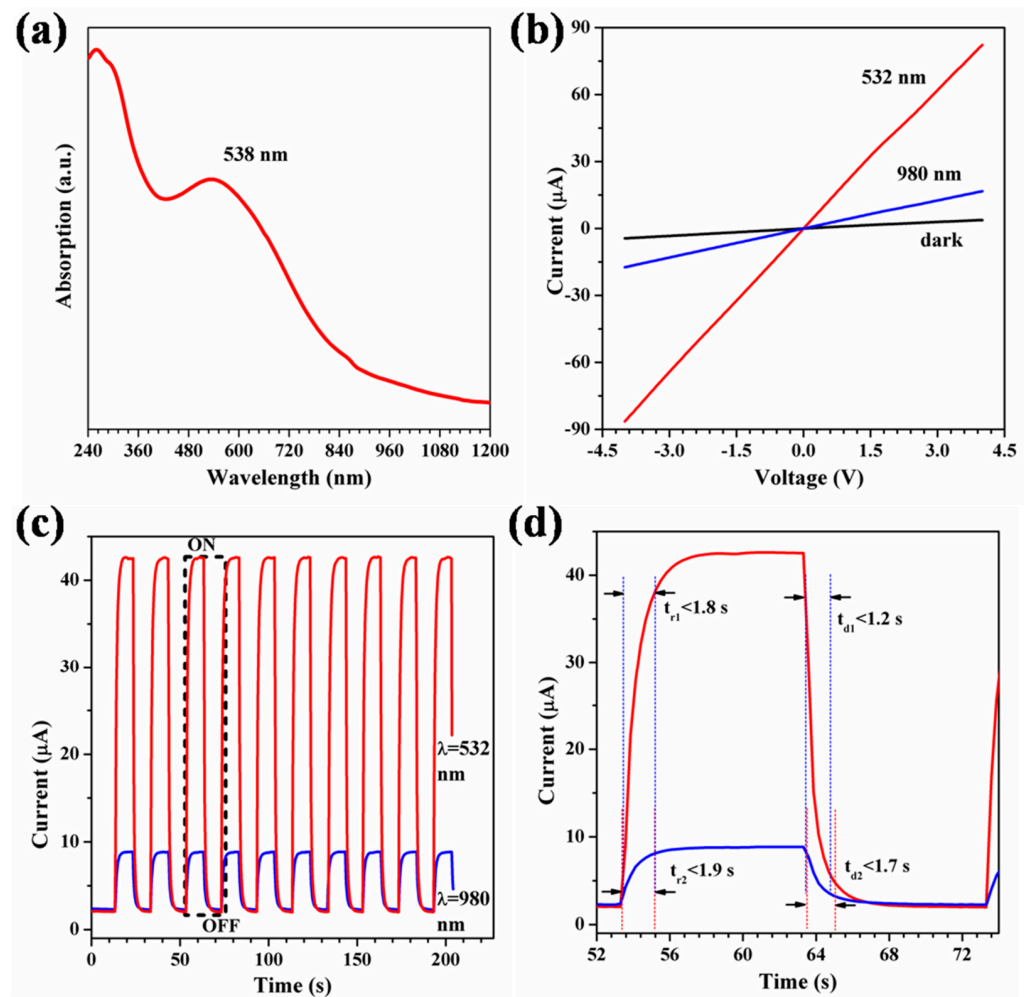


Figure 2. (a) UV-VIS-NR absorption spectrum of tetragonal phase VO₂ (A) nanorods. (b) I–V curves measured in the dark and upon exposure to 532/980 nm illumination, the power densities of 532 nm and 980 nm light are 85 and 120 mW/cm², respectively. (c) Time-dependent photoresponse under periodic illumination at 532 nm and 980 nm wavelengths with intervals of 10 s, applying a bias voltage of 2.0 V, the power densities of 532 nm and 980 nm light are 85 and 120 mW/cm², respectively. (d) An enlarged view of the area enclosed by the black dashed line in (c).

This results in two different current states: a low-current state (in dark) and a high-current state (under illumination). Under visible light (532 nm) irradiation, the photocurrent of the device rises rapidly from 2.1 μA to 42.6 μA, marking a remarkable 1928% increase. Similarly, under infrared light (980 nm) irradiation, the device photocurrent rapidly increases from 2.3 μA to 8.8 μA, resulting in a remarkable 282% increase. Subsequently, when the irradiation of the light source is turned off, the photocurrent drops sharply to its initial level. After the absorption of photons by the tetragonal phase VO₂ (A) NRs, the electrons are transitioned from the valence band to the conduction band, increasing

the concentration of the electrons and holes, which leads to a significant increase in the photocurrent. The currents in both low- and high-current states remained almost constant for 10 cycles, indicating a remarkable reversibility and stability. In comparison to the photodetectors utilizing VO₂ NRs as reported previously, the fabricated devices exhibit exceptional stability and reproducible switching behavior [24,25]. The response speed is a critical property of a photodetector, indicating the speed of the transition between a low-current and high-current state. The response times were defined as the duration taken for the current to increase from 10% to 90% of the maximum photocurrent or decrease from 90% to 10% during the on/off cycle. As illustrated in Figure 2d, the response times (rise and decay times) under visible (532 nm) irradiation are 1.8 s for rise and 1.2 s for decay, while under infrared (980 nm) irradiation for the VO₂ (A) NRs, they are 1.9 s for rise and 1.7 s for decay. The devices exhibit a consistently stable and reproducible light-switching behavior, distinguishing them from the previously reported optical switches based on VO₂ (A) NRs. The rapid response can be attributed to the single-crystal structure of the individual VO₂ (A) NRs and the short current path within the VO₂ (A) NR networks. These properties allow the constructed photodetector to outperform previously reported VO₂ photodetectors, which demonstrated rise and decay times lasting for several seconds [26].

For a more comprehensive analysis of the dynamic response, we investigated the dynamic behavior of the on/off cycle separately under visible and infrared irradiation, respectively. Figure 3a presents a detailed depiction of the response profile for the 'on' cycle, which was subsequently fitted using a stretched exponential function:

$$I = I_0 \left(1 - \exp(-t/\tau_r)^d \right) \quad (1)$$

here, I_0 is the steady state photocurrent, τ_r is the rise time constant, t is the time, and d is an exponent between 0 and 1, which encompasses the characteristics of the relaxation process [27,28]. According to the experimental data and fitting results, the visible (532 nm) and infrared (980 nm) light intensities are 85 mW/cm² and 120 mW/cm² at a bias voltage of 2.0 V. The fitting calculations show that τ_r and d are 0.96 and 0.72, and 0.08 and 0.12 s, respectively. In addition, we analyzed the decrease in the photocurrent from the maximum steady-state value to the minimum dark current when the irradiated light source is turned off (Figure 3b). A second-order exponential decay model was used to fit the data to this process:

$$I = A \exp(-t/\tau_1) + B \exp(-t/\tau_2) \quad (2)$$

herein, the constants A and B represent weighting factors, and τ_1 and τ_2 are relaxation time constants [29,30]. The existence of double time constants indicates the existence of two distinct relaxation pathways, with the contributions of these different relaxation pathways being distinguished by the corresponding weighting factors. Generally, the value of τ_1 is less than τ_2 , thereby τ_1 represents the faster path component (related to bulk processes), while τ_2 represents the more gradual component (related to surface processes). Figure 3b displays the experimental data fitted according to Equation (2) under visible and infrared irradiation, where the values of A , B , τ_1 , and τ_2 under visible irradiation (532 nm) are 48.3, 1.9, 0.52 s, and 3.53 s, respectively. Similarly, under infrared irradiation (980 nm), the values of A , B , τ_1 , and τ_2 are 7.6, 0.6, 0.7 s, and 3.4 s, respectively. A comparison of the photoresponse properties of different semiconductor oxide materials is shown in Table 1. Figure 3c presents the current–voltage (I–V) curves of the photodetector under dark and light conditions (532 nm visible light at different power densities), demonstrating that the measured I–V curves are linear, thus indicating the presence of an ohmic contact between the VO₂ (A) NRs and the gold electrode. Figure 3c illustrates the dark current–voltage (I–V) characteristics of the photodetector and under visible light (532 nm) irradiation at different power densities. The I–V curve displays a distinct linear behavior, indicating that the contact between the VO₂ (A) NR network and the gold electrodes is an ohmic contact. This suggests that the Au electrodes established a solid connection with the VO₂ (A) NR networks, and the junction resistance was comparably lower than the overall resistance

of the device. The illumination led to a significant surge in the photocurrent, especially noticeable at higher voltage biases. This suggests that the gold electrode establishes an ohmic connection to the VO₂ (A) NR networks and that the junction resistance is less than the overall resistance of the device. The VO₂ (A) NR absorbs photons and excites electrons and holes, leading to a large increase in the carrier concentration, which induces a significant increase in the photocurrent, especially at higher voltage biases. At a bias voltage of 4.0 V, the photocurrent exhibited a remarkable increase of approximately 29-fold, rising from 3.8 μA in the dark to 114.4 μA under visible light irradiation (with a light irradiance of 106.2 mW/cm^2). At the same bias voltage, the photocurrent is gradually enhanced with increasing light intensity, which is attributed to the increase in the free carrier concentration in the VO₂ (A) NR. The photocurrent (I) exhibited a clear dependence on the incident light intensity (P) (as illustrated in Figure 3d). This relationship can be expressed as $I \propto P^b$, with the exponent b being influenced by the density of the trap states and is usually less than 1 [31]. In particular, when there is a high trap state density, the lifetime of the photogenerated carriers is shortened, and the photocurrent exhibits a linear departure corresponding to the incident light power. Fitting the experimental data resulted in $I = 0.89$, a non-uniform value that suggests a multifaceted process encompassing electron/hole generation, recombination, and trapping, similar to observations in V₂O₅ nanorods and VO₂ (M1) microwires [7,32].

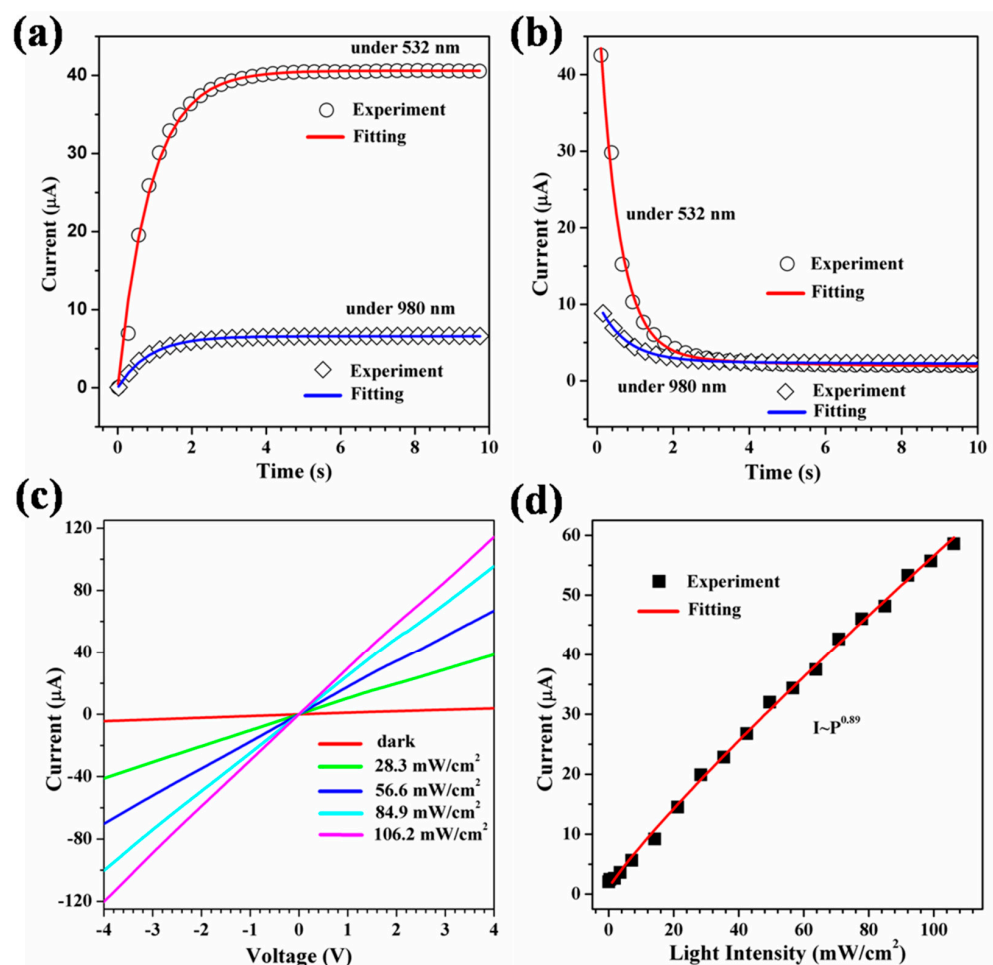


Figure 3. Fitting the (a) response curve and (b) reset curve under illumination at wavelengths of 532 nm and 980 nm, with a bias voltage of 2.0 V, the power densities of 532 nm and 980 nm light are 85 and 120 mW/cm^2 , respectively. (c) I-V curves of the device under 532nm illuminations with different light intensities. (d) Relationship between photocurrent and incident light density at a bias voltage of 2.0 V.

Table 1. The comparison of photoresponse properties for various semiconductor oxide materials.

Photodetector	Laser	τ_r	τ_d	Ref.
VO ₂ (M1) thin film	1550 nm	2.23 s	3.67 s	[33]
ZnO nanowires	365 nm	32 s	3.2 s	[30]
ZnO thin film	365 nm	24 s	15s	[34]
V ₂ O ₅ nanorods	535 nm	0.79 s	0.54 s	[35]
SnO ₂ nanowires	250 nm	0.03 s	0.03 s	[36]
Sb ₂ O ₃ networks	400 nm	0.3 s	0.3 s	[37]
Zn ₂ GeO ₄ networks	254 nm	0.3 s	0.2 s	[6]
VO ₂ (A) NR networks	532 nm	0.96 s	0.52 s	this work
VO ₂ (A) NR networks	980 nm	0.08 s	0.70 s	this work

To investigate the flexibility of the devices, we further fabricated flexible photodetectors using VO₂ NRs on mechanically flexible substrates (PET) as shown in Figure 4a,b. The dynamic photocurrent of the device in the flat state under irradiation with different visible power densities is shown in Figure 4a. At a bias voltage of 2.0 V, the photocurrent increases significantly with the increasing power density of visible irradiation. The ratio of photocurrent to dark current increases from 8.5 times to 27.2 times as the visible irradiation power density increases from 28.3 mW/cm² to 106.2 mW/cm². Figure 4b illustrates the correlation between the dynamic photocurrent and visible irradiation power density in the bent state, with a bias voltage of 2.0 V. The photocurrent increases significantly with increasing visible light irradiation power density when the device is bent at a large angle. Compared to the flat state, the photocurrent magnitude of the device remains almost constant with only slight fluctuations in the bent state for the same visible power density irradiation. The fluctuations in the photocurrent of flexible photodetector devices, in comparison to rigid photodetector devices, can be attributed to the unavoidable rearrangement of the nanowires and contraction sliding between them during bending. Furthermore, the contact between the nanorods, the flexible substrate, and the metal electrodes leads to slight fluctuations in the photocurrent during bending. We also conducted tests on the optoelectronic performance of the flexible device under repeated bending. Even after undergoing numerous repeated bends, the properties of the devices scarcely changed significantly. This can be attributed to the solid contact (ohmic contact) between the closely spaced nanorods and the metal electrodes. These features indicate that our photodetector device has potential applications in the area of flexible electronics.

To explore the surface electron transport mechanism more deeply, we have investigated the dynamic photocurrent of the tetragonal phase VO₂ (A) NR networks under vacuum and atmospheric conditions. Figure 5a shows the I–V curves recorded in the dark. The significant enhancement of the photocurrent under vacuum conditions suggests that reducing the ambient pressure can increase the conductivity. Additionally, this confirms that the adsorption and desorption behavior of the NR surface plays an important role in the photoresponse process. Figure 5b shows the dynamic photocurrent of the device measured in vacuum and air at a bias voltage of 2.0 V and a visible irradiance power density of 85 mW/cm². Under photoirradiation conditions, the photocurrent increases rapidly, from 4.5 to 34.3 μ A (in vacuum) and from 2.1 to 20.4 μ A (in air), and the photocurrent gains of the devices are 662% and 871%, respectively. Fitting the rise and decay of the dynamic photocurrent with Equation (1) (Figure 5c) and Equation (2) (Figure 5d) yields $\tau_r = 0.06$ s (in vacuum) and $\tau_r = 0.13$ s (in air), respectively. Therefore, the presence of oxygen in air accelerates the saturation of the photocurrent, indicating that the surface states of the electron trap are quickly filled with holes. The exponent d was 0.03 (in vacuum) and 0.09 (in air), with corresponding τ_1 values of 1.735 and 0.16 seconds, and τ_2 values of 37.202 and 0.597 s, respectively. As described above, τ_1 represents rapid interband recombination within the bulk, while τ_2 corresponds to surface processes, contingent upon the presence of surface oxygen. Commonly, the inherent potential generated by adsorbed oxygen on the surface of NRs promotes the separation of photogenerated electron–hole pairs, which

leads to the accumulation of holes on the NR surface [38]. Therefore, the electron–hole recombination indirectly on the NR surface possesses a prolonged time constant.

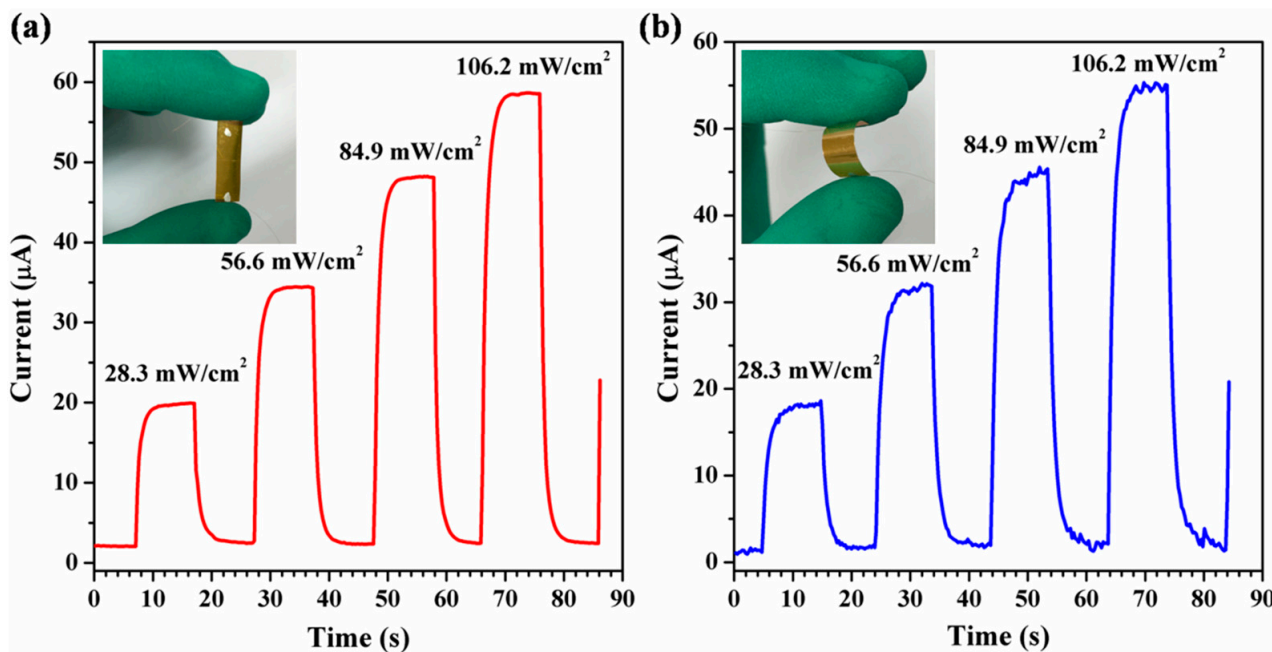


Figure 4. Time-dependent photoresponse to visible light (532 nm) at different irradiation intensities under periodic illumination at 10 s intervals, applying a bias voltage of 2.0 V, the inset image shows an optical picture of the test device. (a) Flat condition test. (b) Bending condition test.

The photodetection mechanism of the VO₂ (A) NR networks includes the production of free charge carriers and their subsequent transportation, encompassing interfaces between neighboring nanorods and the metal/VO₂ (A) interface. The surface states of the device, including vacancies, surface defects, and dangling bonds in the VO₂ (A) NRs, can affect the generation and quantity of free charge carriers. The adsorption effect of the surface states has been reported in many photodetector devices based on oxide semiconductor nanowire networks, such as ZnO nanodisk [39], Zn₂GeO₄ nanowire networks [6], and so on. The VO₂ (A) NRs exhibit n-type semiconductor behavior, with oxygen vacancies contributing electrons to the conduction band. Thus, the fundamental photodetection mechanism of these nanorods involves the adsorption and desorption of oxygen molecules, which modulates the production of free charge carriers and electron transport.

In the dark, absorbed oxygen molecules capture electrons on the surface of the nanorods, generating surface states with negative charges (or oxygen ions) [$O_2(g) + e^- \rightarrow O_2^-(ad)$], causing a depletion layer to form near the surface, which reduces the electrical conductivity. The electron–hole pairs [$h\nu \rightarrow e^- + h^+$] generated due to visible light illumination are then separated by the surface electric field. The additional holes migrate toward the nanorod surface following the potential gradient and combine with oxygen, leading to oxygen desorption from the surface of the VO₂ (A) NR [$h^+ + O_2^-(ad) \rightarrow O_2(g)$] (Figure 6a). This increases the quantity of the unpaired electrons, raises the carrier concentration, and reduces the width of the depletion layer, resulting in a notable increase in the photocurrent. According to the literature reports, the adsorption and desorption of oxygen molecules play a key in influencing the photoconductivity of metal oxide semiconductors, including Zn₂GeO₄, SnO₂, and ZnO [40,41]. Furthermore, the nanorods network structure may have an additional conduction mechanism that is absent in single nanorod devices. The resistance between two intersecting nanorods mainly originates from the impedance of the NR–NR junction rather than the effect of the intrinsic resistance of the NR. This junction barrier located near the surface of the NRs results in

a significant band bending (Figure 6b), and the charge carriers have to pass through the junction barrier. In NR network photodetectors, the NR–NR junction barrier must be overcome when the electrons are transported from one nanorod (NR) to another (NR) (as shown in Figure 6c). The barrier to electron transfer arises from the surface depletion layer, which can be reduced by light due to the increase in carrier density, thus effectively lowering the effective barrier height. Under illumination, the height of the barrier potential of the NR–NR junction decreases, making it easier for charge carriers to pass through the NR network, resulting in an increase in the photocurrent. The modulation of the barrier height induced by light has been observed in optoelectronic devices utilizing nanobelts and nanowire networks as well [42,43].

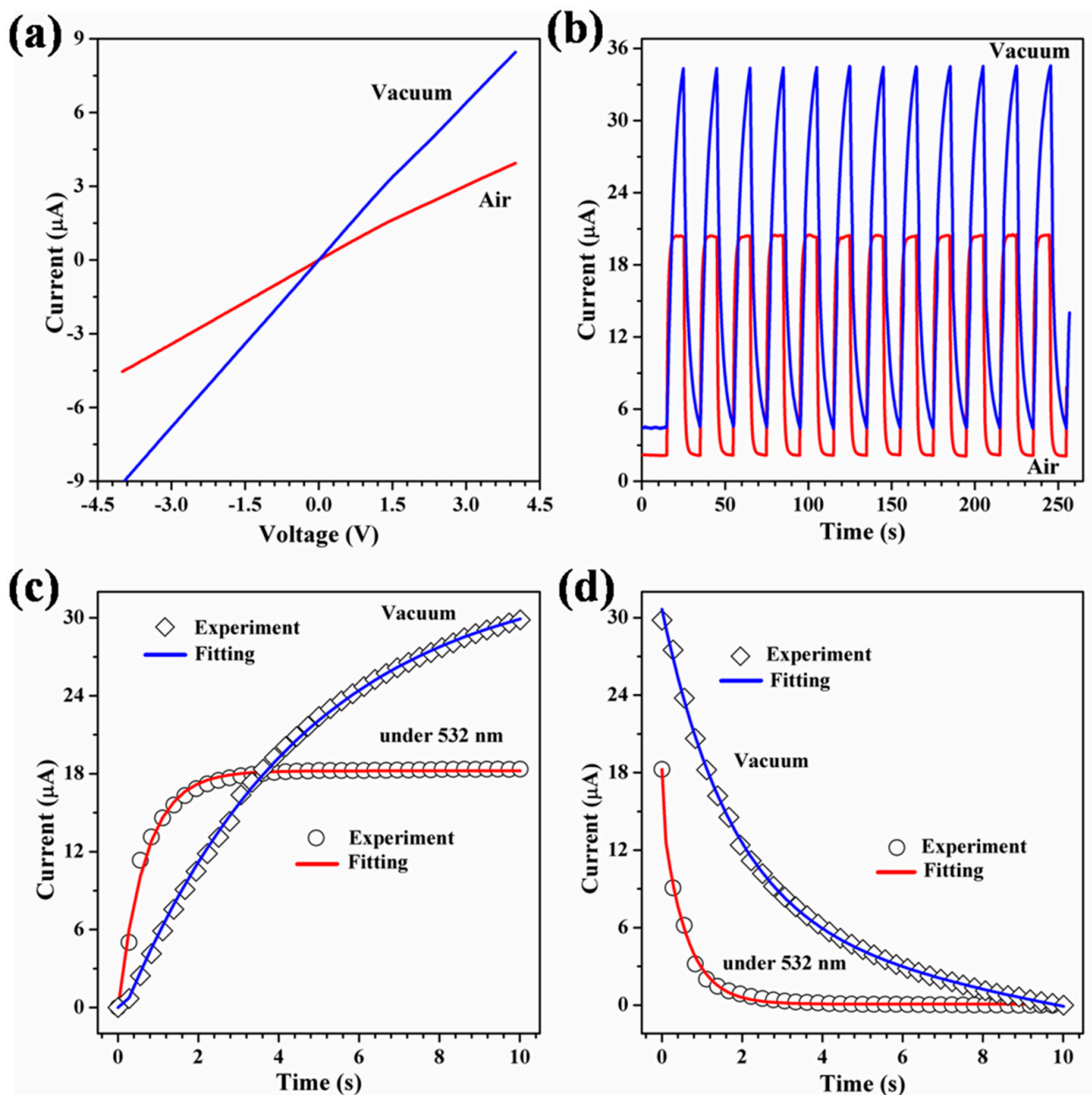


Figure 5. (a) I–V characteristics of the device in both air and vacuum in the dark. (b) Time-dependent photoresponse in both air and vacuum at 10 s intervals under periodic light illumination with a bias voltage of 2.0 V (light intensity 28.3 mW/cm²). (c) Fitting the response curve and (d) reset under light illumination in air and vacuum in the dark, applying a bias voltage of 2.0 V, the power densities of visible is 28.3 mW/cm².

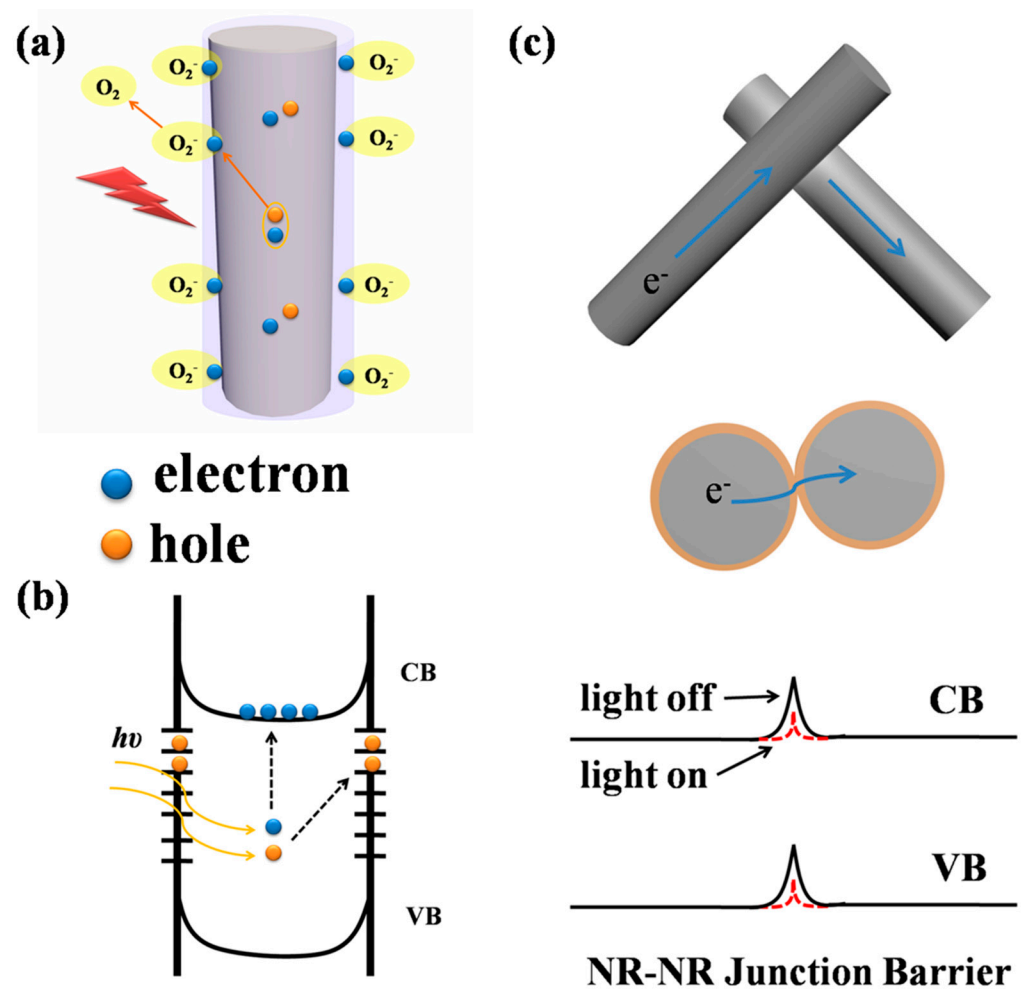


Figure 6. (a) Schematic depiction of oxygen adsorption in the dark and oxygen desorption upon nanorod illumination. (b) Excitation of hole and carrier jumps after photon absorption by nanorods. (c) Junction barrier for electron transport between nanorods (NR-NR) and its modification upon illumination.

4. Conclusions

In conclusion, single crystalline tetragonal phase VO₂ (A) NRs were synthesized using a hydrothermal method. We have demonstrated that tetragonal phase VO₂ (A) NR networks can be utilized to construct efficient flexible photodetectors. This method is straightforward, cost-effective, and does not require a complex lithography process. The devices exhibit exceptional photosensitivity, reproducibility, and stability under ambient conditions. With a bias voltage of 2.0 volts, the device demonstrates a photocurrent switching gain of 1982% and 282% under irradiation with light at wavelengths of 532 nm and 980 nm, respectively. The devices show a fast photoelectric response with rise times of 1.8 s and 1.9 s and decay times of 1.2 s and 1.7 s for light at wavelengths of 532 nm and 980 nm, respectively. The fabricated devices exhibit rapid response and recovery times, attributed to the predominant carrier transmission through NR-NR junctions. The dynamic response behavior suggests a mechanism for the modulation of the barrier height induced by light. The results from multiple large-angle bending experiments demonstrate that the device possesses excellent flexibility characteristics. This simple photodetector fabrication technique provides a promising path for manufacturing low-cost, high-performance, large-scale flexible wearable devices based on nanomaterials.

Author Contributions: W.L. and C.T. contributed equally to this work; writing—original draft preparation, W.L. and C.T.; methodology, F.W., Q.W. and Y.Z. (Yiyu Zhu); investigation, Z.W. and Y.L.; formal analysis, C.T. and F.W.; data curation, Q.W., Y.L. and S.L.; writing—review and editing, J.H., Y.Z. (Yi Zhang) and W.L.; validation, Z.W. and Y.Z. (Yiyu Zhu); supervision, J.H. and S.L.; project administration, J.H.; funding acquisition, J.H. and Y.Z. (Yi Zhang). All authors have read and agreed to the published version of the manuscript.

Funding: The work was supported by the National Natural Science Foundation of China (52002170), the Natural Science Foundation of Jiangsu Province (BK20190687), the State Key Laboratory of Materials-Oriented Chemical Engineering (No. KL19-03), and the Postgraduate Research & Practice Innovation Program of Jiangsu Province (KYCX23_1429).

Institutional Review Board Statement: Not applicable.

Informed Consent Statement: Not applicable.

Data Availability Statement: Not applicable.

Conflicts of Interest: The authors declare no conflict of interest.

References

1. Balandin, A.A.; Kargar, F.; Salguero, T.T.; Lake, R.K. One-dimensional van der Waals quantum materials. *Mater. Today* **2022**, *55*, 74–91. [[CrossRef](#)]
2. Pham, T.; Qamar, A.; Dinh, T.; Masud, M.K.; Rais-Zadeh, M.; Senesky, D.G.; Yamauchi, Y.; Nguyen, N.T.; Phan, H.P. Nanoarchitectonics for wide bandgap semiconductor nanowires: Toward the next generation of nanoelectromechanical systems for environmental monitoring. *Adv. Sci.* **2020**, *7*, 2001294. [[CrossRef](#)] [[PubMed](#)]
3. Ahoulou, S.; Perret, E.; Nedelec, J.-M. Functionalization and characterization of silicon nanowires for sensing applications: A review. *Nanomaterials* **2021**, *11*, 999. [[CrossRef](#)] [[PubMed](#)]
4. Fast, J.; Aeberhard, U.; Bremner, S.P.; Linke, H. Hot-carrier optoelectronic devices based on semiconductor nanowires. *Appl. Phys. Rev.* **2021**, *8*, 021309. [[CrossRef](#)]
5. Kumaresan, Y.; Min, G.B.; Dahiya, A.S.; Ejaz, A.; Shakthivel, D.; Dahiya, R. Kirigami and Mogul-patterned ultra-stretchable high-performance ZnO nanowires-based photodetector. *Adv. Mater. Technol.* **2022**, *7*, 2100804. [[CrossRef](#)]
6. Yan, C.; Singh, N.; Lee, P.S. Wide-bandgap Zn₂GeO₄ nanowire networks as efficient ultraviolet photodetectors with fast response and recovery time. *Appl. Phys. Lett.* **2010**, *96*, 053108. [[CrossRef](#)]
7. Fu, W.B.; Shang, G.L.; Gong, X.X.; Zhang, L.D.; Fei, G.T. Preparation of large scale and highly ordered vanadium pentoxide nanowire arrays towards high performance photodetectors. *J. Mater. Chem. C* **2017**, *5*, 1474–1478. [[CrossRef](#)]
8. Hou, J.; Wang, X.; Fu, D.; Ko, C.; Chen, Y.; Sun, Y.; Lee, S.; Wang, K.X.; Dong, K.; Sun, Y.; et al. Modulating photoluminescence of monolayer molybdenum disulfide by metal-insulator phase transition in active substrates. *Small* **2016**, *12*, 3976–3984. [[CrossRef](#)]
9. Manca, N.; Kanki, T.; Endo, F.; Marré, D.; Pellegrino, L. Planar nanoactuators based on VO₂ phase transition. *Nano Lett.* **2020**, *20*, 7251–7256. [[CrossRef](#)]
10. Huber, M.A.; Plankl, M.; Eisele, M.; Marvel, R.E.; Sandner, F.; Korn, T.; Schüller, C.; Haglund, R.F., Jr.; Huber, R.; Cocker, T.L. Ultrafast mid-infrared nanoscopy of strained vanadium dioxide nanobeams. *Nano Lett.* **2016**, *16*, 1421–1427. [[CrossRef](#)]
11. Hou, J.; Zhang, J.; Wang, Z.; Zhang, Z.; Ding, Z. Structural transition of VO₂ (A) nanorods studied by vibrational spectroscopies. *RSC Adv.* **2014**, *4*, 18055–18060. [[CrossRef](#)]
12. Majid, S.S.; Ahad, A.; Rahman, F.; Sathe, V.; Shukla, D. Unveiling the role of VO₂ (B) polymorph in the insulator-metal transition of VO₂ (M1) thin films. *Phys. Status Solidi B* **2022**, *259*, 2200108. [[CrossRef](#)]
13. Lee, S.; Sun, X.-G.; Lubimtsev, A.A.; Gao, X.; Ganesh, P.; Ward, T.Z.; Eres, G.; Chisholm, M.F.; Dai, S.; Lee, H.N. Persistent electrochemical performance in epitaxial VO₂(B). *Nano Lett.* **2017**, *17*, 2229–2233. [[CrossRef](#)]
14. Schofield, P.; Bradicich, A.; Gurrola, R.M.; Zhang, Y.W.; Brown, T.D.; Pharr, M.; Shamberger, P.J.; Banerjee, S. Harnessing the metal-insulator transition of VO₂ in neuromorphic computing. *Adv. Mater.* **2023**, *35*, 2205294. [[CrossRef](#)] [[PubMed](#)]
15. Liu, K.; Lee, S.; Yang, S.; Delaire, O.; Wu, J. Recent progresses on physics and applications of vanadium dioxide. *Mater. Today* **2018**, *21*, 875–896. [[CrossRef](#)]
16. Choi, S.; Ahn, G.; Moon, S.J.; Lee, S. Tunable resistivity of correlated VO₂(A) and VO₂(B) via tungsten doping. *Sci. Rep.* **2020**, *10*, 9721. [[CrossRef](#)]
17. Zhang, Y.F.; Huang, Y.F.; Zhang, J.C.; Wu, W.B.; Niu, F.; Zhang, Y.L.; Liu, X.H.; Liu, X.; Huang, C. Facile synthesis, phase transition, optical switching and oxidation resistance properties of belt-like VO₂ (A) and VO₂ (M) with a rectangular cross section. *Mater. Res. Bull.* **2012**, *47*, 1978–1986. [[CrossRef](#)]
18. Liang, J.; Wang, K.; Xuan, C.; Chen, Q.; Tai, W.; Ge, P.; Zhang, H. Room temperature H₂S gas sensing performance of VO₂(A) nanowires with high aspect ratio. *Sens. Actuators A Phys.* **2022**, *347*, 113986. [[CrossRef](#)]

19. Samanta, S.; Li, Q.J.; Cheng, B.Y.; Huang, Y.W.; Pei, C.Y.; Wang, Q.L.; Ma, Y.Z.; Wang, L. Phase coexistence and pressure-temperature phase evolution of VO₂ (A) nanorods near the semiconductor-semiconductor transition. *Phys. Rev. B* **2017**, *95*, 045135. [[CrossRef](#)]
20. Popuri, S.R.; Artemenko, A.; Labrugere, C.; Miclau, M.; Villesuzanne, A.; Pollet, M. VO₂ (A): Reinvestigation of crystal structure, phase transition and crystal growth mechanisms. *J. Solid State Chem.* **2014**, *213*, 79–86. [[CrossRef](#)]
21. Jiang, J.; Chen, Z.; Hu, Y.; Xiang, Y.; Zhang, L.; Wang, Y.; Wang, G.-C.; Shi, J. Flexo-photovoltaic effect in MoS₂. *Nat. Nanotechnol.* **2021**, *16*, 894–901. [[CrossRef](#)]
22. Zhang, S.; Shang, B.; Yang, J.; Yan, W.; Wei, S.; Xie, Y. From VO₂ (B) to VO₂ (A) nanobelts: First hydrothermal transformation, spectroscopic study and first principles calculation. *Phys. Chem. Chem. Phys.* **2011**, *13*, 15873–15881. [[CrossRef](#)] [[PubMed](#)]
23. Rogalski, A.; Bielecki, Z.; Mikołajczyk, J.; Wojtas, J. Ultraviolet photodetectors: From photocathodes to low-dimensional solids. *Sensors* **2023**, *23*, 4452. [[CrossRef](#)] [[PubMed](#)]
24. Xie, B.H.; Fu, W.B.; Fei, G.T.; Xu, S.H.; Gao, X.D.; Zhang, L.D. Preparation and enhanced infrared response properties of ordered W-doped VO₂ nanowire array. *Appl. Surf. Sci.* **2018**, *436*, 1061–1066. [[CrossRef](#)]
25. Yin, H.; Ni, J.; Jiang, W.; Zhang, Z.; Yu, K. Synthesis, field emission and humidity sensing characteristics of monoclinic VO₂ nanostructures. *Phys. E Low-dimens. Syst. Nanostructures* **2011**, *43*, 1720–1725. [[CrossRef](#)]
26. Yoon, J.; Hong, W.-K.; Kim, Y.; Park, S.-Y. Nanostructured vanadium dioxide materials for optical sensing applications. *Sensors* **2023**, *23*, 6715. [[CrossRef](#)]
27. Li, L.; Lee, P.S.; Yan, C.; Zhai, T.; Fang, X.; Liao, M.; Koide, Y.; Bando, Y.; Golberg, D. Ultrahigh-performance solar-blind photodetectors based on individual single-crystalline In₂Ge₂O₇ nanobelts. *Adv. Mater.* **2010**, *22*, 5145–5149. [[CrossRef](#)]
28. Aga, R.S.; Jowhar, D.; Ueda, A.; Pan, Z.; Collins, W.E.; Mu, R.; Singer, K.D.; Shen, J. Enhanced photoresponse in ZnO nanowires decorated with CdTe quantum dot. *Appl. Phys. Lett.* **2007**, *91*, 232108. [[CrossRef](#)]
29. Zhang, Y.; Chen, X.; Xu, Y.; Gong, H.; Yang, Y.; Ren, F.-F.; Liu, B.; Gu, S.; Zhang, R.; Ye, J. Anion engineering enhanced response speed and tunable spectral responsivity in gallium-oxynitrides-based ultraviolet photodetectors. *ACS Appl. Electron. Mater.* **2020**, *2*, 808–816. [[CrossRef](#)]
30. Yan, C.; Wang, J.; Wang, X.; Kang, W.; Cui, M.; Foo, C.Y.; Lee, P.S. An intrinsically stretchable nanowire photodetector with a fully embedded structure. *Adv. Mater.* **2014**, *26*, 943–950. [[CrossRef](#)]
31. Afal, A.; Coskun, S.; Unalan, H.E. All solution processed, nanowire enhanced ultraviolet photodetectors. *Appl. Phys. Lett.* **2013**, *102*, 043503. [[CrossRef](#)]
32. Wu, J.M.; Chang, W.E. Ultrahigh responsivity and external quantum efficiency of an ultraviolet-light photodetector based on a single VO₂ microwire. *ACS Appl. Mater. Interfaces* **2014**, *6*, 14286–14292. [[CrossRef](#)] [[PubMed](#)]
33. Rajeswaran, B.; Tadeo, I.J.; Umarji, A.M. IR photoresponsive VO₂ thin films and electrically assisted transition prepared by single-step chemical vapor deposition. *J. Mater. Chem. C* **2020**, *8*, 12543–12550. [[CrossRef](#)]
34. Sun, M.; Xu, Z.; Yin, M.; Lin, Q.; Lu, L.; Xue, X.; Zhu, X.; Cui, Y.; Fan, Z.; Ding, Y.; et al. Broad-band three dimensional nanocave ZnO thin film photodetectors enhanced by Au surface plasmon resonance. *Nanoscale* **2016**, *8*, 8924–8930. [[CrossRef](#)] [[PubMed](#)]
35. Abd-Alghafour, N.M.; Ahmed, N.M.; Hassan, Z. Fabrication and characterization of V₂O₅ nanorods based metal–semiconductor–metal photodetector. *Sens. Actuators A Phys.* **2016**, *250*, 250–257. [[CrossRef](#)]
36. Gan, L.; Liao, M.; Li, H.; Ma, Y.; Zhai, T. Geometry-induced high performance ultraviolet photodetectors in kinked SnO₂ nanowires. *J. Mater. Chem. C* **2015**, *3*, 8300–8306. [[CrossRef](#)]
37. Li, L.; Zhang, Y.X.; Fang, X.S.; Zhai, T.Y.; Liao, M.Y.; Wang, H.Q.; Li, G.H.; Koide, Y.; Bando, Y.; Golberg, D. Sb₂O₃ nanobelt networks for excellent visible-light-range photodetectors. *Nanotechnology* **2011**, *22*, 165704. [[CrossRef](#)]
38. Nasiri, N.; Jin, D.; Tricoli, A. Nanoarchitectonics of visible-blind ultraviolet photodetector materials: Critical features and nano-microfabrication. *Adv. Opt. Mater.* **2019**, *7*, 1800580. [[CrossRef](#)]
39. Alenezi, M.R.; Alshammari, A.S.; Alzanki, T.H.; Jarowski, P.; Henley, S.J.; Silva, S.R.P. ZnO nanodisk based UV detectors with printed electrodes. *Langmuir* **2014**, *30*, 3913–3921. [[CrossRef](#)]
40. Praveen, S.; Veeralingam, S.; Badhulika, S. A flexible self-powered UV photodetector and optical UV filter based on β-Bi₂O₃/SnO₂ quantum dots Schottky heterojunction. *Adv. Mater. Interfaces* **2021**, *8*, 2100373. [[CrossRef](#)]
41. Ouyang, W.; Chen, J.; Shi, Z.; Fang, X. Self-powered UV photodetectors based on ZnO nanomaterials. *Appl. Phys. Rev.* **2021**, *8*, 031315. [[CrossRef](#)]
42. Mathews, N.; Varghese, B.; Sun, C.; Thavasi, V.; Andreasson, B.P.; Sow, C.H.; Ramakrishna, S.; Mhaisalkar, S.G. Oxide nanowire networks and their electronic and optoelectronic characteristics. *Nanoscale* **2010**, *2*, 1984–1998. [[CrossRef](#)] [[PubMed](#)]
43. Arquer, F.P.; Armin, A.; Meredith, P.; Sargent, E.H. Solution-processed semiconductors for next-generation photodetectors. *Nat. Rev. Mater.* **2017**, *2*, 16100. [[CrossRef](#)]

Disclaimer/Publisher’s Note: The statements, opinions and data contained in all publications are solely those of the individual author(s) and contributor(s) and not of MDPI and/or the editor(s). MDPI and/or the editor(s) disclaim responsibility for any injury to people or property resulting from any ideas, methods, instructions or products referred to in the content.